Title

The effect of different solar wind parameters upon significant relativistic electron flux dropouts in the magnetosphere

Journal

Journal of Geophysical Research Space Physics, 120(6)

ISSN

2169-9380

Authors

Gao, Xinliang
Li, Wen
Bortnik, Jacob
et al.

Publication Date

2015-06-01

DOI

10.1002/2015ja021182

Peer reviewed

AGU PUBLICATIONS

JGR

Journal of Geophysical Research: Space Physics

RESEARCH ARTICLE
10.1002/2015JA021182

Key Points:
- Either large *P* or southward IMF B_z alone is capable of causing electron dropouts
- Large P pushes magnetopause inward strongly and causes magnetopause shadowing
- Strong southward IMF B_z causes stronger electron precipitation in dusk sector

Correspondence to:
X. Gao,
gaoxl@mail.ustc.edu.cn

Citation:
Gao, X., W. Li, J. Bortnik, R. M. Thorne, Q. Lu, Q. Ma, X. Tao, and S. Wang (2015), The effect of different solar wind parameters upon significant relativistic electron flux dropouts in the magnetosphere, *J. Geophys. Res. Space Physics*, *120*, 4324–4337, doi:10.1002/2015JA021182.

Received 2 MAR 2015
Accepted 7 MAY 2015
Accepted article online 10 MAY 2015
Published online 3 JUN 2015

The effect of different solar wind parameters upon significant relativistic electron flux dropouts in the magnetosphere

Xinliang Gao[1,2], Wen Li[3], Jacob Bortnik[3], Richard M. Thorne[3], Quanming Lu[1,2], Qianli Ma[3], Xin Tao[1,2], and Shui Wang[1,2]

[1]CAS Key Laboratory of Geospace Environment, Department of Geophysics and Planetary Science, University of Science and Technology of China, Hefei, China, [2]Collaborative Innovation Center of Astronautical Science and Technology, Harbin, China, [3]Department of Atmospheric and Oceanic Sciences, UCLA, Los Angeles, California, USA

Abstract Superposed epoch analyses were performed on 193 significant relativistic electron flux dropout events, in order to study the roles of different solar wind parameters in driving the depletion of relativistic electrons, using ~16 years of data from the POES and GOES missions, and the OMNIWEB solar wind database. We find that the solar wind dynamic pressure and interplanetary magnetic field (IMF) B_z play key roles in causing the relativistic electron flux dropouts, but also that either large solar wind dynamic pressure or strong southward IMF B_z by itself is capable of producing the significant depletion of relativistic electrons. The relativistic electron flux dropouts occur not only when the magnetopause is compressed closer to the Earth but also when the magnetopause is located very far ($>$ ~10 R_E). Importantly, our results show that in addition to the large solar wind dynamic pressure, which pushes the magnetopause inward strongly and causes the electrons to escape from the magnetosphere, relativistic electrons can also be scattered into the loss cone and precipitate into the Earth's atmosphere during periods of strong southward IMF B_z, which preferentially provides a source of free energy for electromagnetic ion cyclotron (EMIC) wave excitation. This is supported by the fact that the strongest electron precipitation into the atmosphere is found in the dusk sector, where EMIC waves are typically observed in the high-density plasmasphere or plume and cause efficient electron precipitation down to ~1 MeV.

1. Introduction

Since its discovery in 1958 by the Explorer series of spacecraft [*Van Allen and Frank*, 1959], the Van Allen radiation belts have drawn extensive attention and intense scientific interest [*Bortnik and Thorne*, 2007; *Millan and Thorne*, 2007; *Summers et al.*, 2007; *Thorne*, 2010; *Baker and Blake*, 2012; *Turner et al.*, 2012; *Thorne et al.*, 2013]. The Earth's radiation belts, which consist of an inner belt and an outer belt, are filled with trapped relativistic electrons, which have a great impact on spacecraft systems [*Baker*, 2002], astronauts [*Maalouf et al.*, 2011], and as polar atmospheric chemistry [*Randall et al.*, 2005]. Understanding their evolution is an indispensable part of space weather prediction. However, these energetic electrons in the outer radiation belt can be highly dynamic with observed fluxes varying by several orders of magnitude on time scales of hours to days [*Summers et al.*, 2007; *Shprits et al.*, 2009; *Selesnick and Kanekal*, 2009; *Kim et al.*, 2011; *Turner et al.*, 2012; *Thorne et al.*, 2013; *Yuan and Zong*, 2013; *Li et al.*, 2014]. Although the radiation belts have been studied for over four decades [*Van Allen and Frank*, 1959; *Parker*, 1960; *Freden and White*, 1960; *Thorne and Kennel*, 1971; *Lyons and Thorne*, 1972; *Millan and Thorne*, 2007; *Turner et al.*, 2012], many of the processes responsible for the evolution of the outer belt are still not fully understood due to the combined effects of electron acceleration and loss. For instance, similar geomagnetic storms can produce dramatically different results in terms of enhancing or depleting radiation belt electron fluxes [*Reeves et al.*, 2003]. In this paper, we focus primarily on the relativistic electron flux dropout events, which are often observed during geomagnetic storms [*Onsager et al.*, 2002; *Reeves et al.*, 2003; *Turner et al.*, 2012].

Both theoretical and observational studies of relativistic electron losses have shown that the observed decreases in the trapped electron flux can be caused by reversible adiabatic effects [*Mcilwain*, 1966; *Millan and Thorne*, 2007], or permanent losses through either precipitation into the atmosphere [*Bortnik et al.*,

2006; *Shprits et al.*, 2006, 2012; *Millan et al.*, 2007; *Jordanova et al.*, 2008; *Turner et al.*, 2014] or magnetopause shadowing [*Bortnik et al.*, 2006; *Kim et al.*, 2010; *Turner et al.*, 2012, 2014; *Yuan and Zong*, 2013]. One of the most promising mechanisms for driving rapid electron loss is magnetopause shadowing, which is caused by the sudden inward movement of the magnetopause [*Bortnik et al.*, 2006; *Turner et al.*, 2012, 2014; *Yuan and Zong*, 2013]. In this scenario, when electrons are drifting around the Earth, they encounter the compressed magnetopause and escape from the magnetosphere. Moreover, the subsequent outward radial diffusion can result in further losses toward the magnetopause and cause the decrease in electron fluxes deep into low L shells.

In addition to being lost to the magnetopause, electrons can also be scattered into the loss cone and precipitate into the Earth's atmosphere [*Bortnik et al.*, 2006; *Millan et al.*, 2007; *Millan and Thorne*, 2007; *Turner et al.*, 2014]. Relativistic electrons can be pitch angle scattered through resonant interactions with different plasma waves, including whistler mode chorus waves observed outside the plasmaspause preferentially in the dawn sector and electromagnetic ion cyclotron (EMIC) waves usually observed in the plasmaspheric plume region in the dusk sector. Whistler mode chorus is able to scatter approximately MeV electrons if their interactions take place off the equator [*Thorne et al.*, 2005]. While, EMIC waves can scatter approximately MeV electrons strongly in a limited range of local time (e.g., near the dusk sector), where the plasma density is high and thus lowers the minimum resonant energy [e.g., *Li et al.*, 2007]. Moreover, previous works have already provided the simultaneous observations of the relativistic electron precipitation and the occurrence of EMIC waves [*Rodger et al.*, 2008; *Carson et al.*, 2013; *Wang et al.*, 2014]. Another possible way of causing loss of energetic electrons to the Earth's atmosphere is through current sheet scattering [*Sergeev and Tsyganenko*, 1982], which occurs when the electron gyro radius is comparable to the curvature radius of the magnetic field. This mechanism takes place mainly on the nightside, where the tail-like magnetic field lines occur and have the smaller curvature radius. This mechanism will act selectively on higher-energy particles such as relativistic electrons (approximately MeV), since their gyro radii are larger than those of lower-energy particles. This phenomenon has also been observed by the low-altitude satellites [*Imhof et al.*, 1991].

Most studies on relativistic electron flux dropouts have focused on events that occur during geomagnetic storms driven by either corotating interaction regions [*Denton and Borovsky*, 2008; *Borovsky and Denton*, 2009, 2010; *Morley et al.*, 2010a, 2010b; *Meredith et al.*, 2011] or coronal mass ejections [*Bortnik et al.*, 2006; *Turner et al.*, 2012; *Yuan and Zong*, 2013], although some studies have shown that relativistic electron flux dropouts can occur even without a geomagnetic storm [*Green et al.*, 2004; *Ohtani et al.*, 2009]. Using a superposed epoch analysis on the dropout events, previous studies showed that there are usually enhancements of the solar wind dynamic pressure and southward interplanetary magnetic field (IMF) B_z that accompany the depletion of relativistic electrons [*Denton and Borovsky*, 2008; *Borovsky and Denton*, 2010; *Yuan and Zong*, 2013]. In addition, satellite observations demonstrated that during most of the relativistic electron flux dropouts, the electron fluxes do not recover to their previous levels even after the geomagnetic conditions have substantially recovered [*Bortnik et al.*, 2006; *Turner et al.*, 2012]. To explain this permanent loss of relativistic electrons during flux dropouts, either magnetopause shadowing or wave-particle interaction has been proposed based on observations and simulations, but there is still no consensus in the community regarding when and where each mechanism is dominant. Although the solar wind dynamic pressure and southward IMF B_z are believed to play an important role in causing the relativistic electron flux dropout, their relative roles are still not clear.

In this study we provide a comprehensive investigation into the effects of different solar wind parameters in causing significant relativistic electron flux dropout events. While other studies have only focused on the dropout events during geomagnetic storms, this study investigates ~16 years of data from six polar orbiting satellites and eight geosynchronous spacecraft regardless of whether a geomagnetic storm occurs or not. In section 2 we describe the data sets used in this study. Section 3.1 describes the method used for identifying and classifying the events, and the statistical features of the events using a superposed epoch analysis are shown in section 3.2. In sections 4 and 5, we summarize and further discuss our principal results.

2. Instrument and Data Sets

The 1 min average values of electron fluxes with energies >0.6 MeV and >2 MeV at geosynchronous Earth orbit (GEO) are provided by the Energetic Particle Sensor instrument on board the Geostationary

Operational Environment Satellites (GOES) [*Onsager et al.*, 1996]. For the present study, large amounts of data from July 1998 to April 2014 are analyzed to identify the dropout events from eight GOES satellites (from GOES 8 to GOES 15).

To complement the geosynchronous measurements, we also utilize electron measurements from the Medium Energy Proton and Electron Detector (MEPED) on board the NOAA Polar Orbiting Environmental Satellites (POES 15–19) and European Organization for the Exploitation of Meteorological Satellites Meteorological Operational (MetOp) satellites (MetOp 02). These Sun-synchronous satellites orbit at a low altitude (~800 km) and fly around the Earth about every 100 min. The MEPED instrument is equipped with two perpendicular electron solid-state detector telescopes: T0, called the 0° telescope, is mounted aligned so that the center of its field of view is approximately outward along the local zenith; T90, called the 90° telescope, is placed perpendicular so that the center of its field of view is antiparallel to the spacecraft velocity [*Evans and Greer*, 2004]. Besides, three energy bands are designed to measure the flux of electrons from 30 keV to 2500 keV [*Evans and Greer*, 2004; *Green*, 2013]. Since the local bounce loss cone (~59°) is much larger than the field of view of each telescope (~30°) at the altitude of the POES/MetOp satellites, the T0 telescope can measure the precipitating flux inside the loss cone at $L > 1.4$ [*Rodger et al.*, 2010], and the T90 telescope mostly measures the geomagnetically trapped flux with the invariant latitude from 55° to 70° [*Meredith et al.*, 2011]. In this paper, we analyze the electron flux obtained from four energy channels, the $30 < E < 2500$ keV, $100 < E < 2500$ keV, $300 < E < 2500$ keV, and $E >$ ~1 MeV. The flux of relativistic electrons ($E >$ ~1 MeV) is obtained from the $E > 6900$ keV proton channel [*Sandanger et al.*, 2009; *Green*, 2013]. For convenience, we henceforth refer to them as the $E > 30$ keV, $E > 100$ keV, $E > 300$ keV, and $E > 1$ MeV channels, respectively. The proton contamination has been removed following the correction procedure described in *Lam et al.* [2010].

To supplement the energetic electron data, 1 min averages of solar wind and IMF measurements data are obtained from the OMNIWEB database (http://omniweb.gsfc.nasa.gov), which combines solar wind observations taken by the different spacecraft including the IMP 8, Wind, and ACE spacecraft. All the data have been time shifted from their spacecraft locations to the bow shock nose with the technique explained at http://omniweb.gsfc.nasa.gov/html/HROdocum.html [*Bargatze et al.*, 2005; *Weimer and King*, 2008]. Some geomagnetic indices, such as *AE*, *AL*, and *Dst*, are also obtained from the OMNIWEB database. *Kp* index is provided by the World Data Center, Kyoto, Japan.

3. Observational Results

3.1. Event Identification and Classification

In order to select all the significant electron flux dropout events, we have examined the 16 year electron (>2 MeV) flux data obtained from eight GOES satellites. Our selection procedure is developed based on the method used in the study of *Green et al.* [2004]. We first conduct a 2 h smoothing on these data and then calculate the ratio between the electron flux at the current time (f_c) and the flux level 24 h prior to it (f_p) for each geosynchronous satellite. The ratio essentially compares the flux measured at identical local times. An electron flux dropout event is recorded when this flux ratio drops below 0.01. The onset of the event is found by moving back in time until the ratio equals to 0.5, and its end is defined as the time when the ratio reaches its maximum within 2 days after the onset. In this study, only significant dropout events are considered by requiring that the mean electron flux on one day after the onset must be lower than 12.5% of that on 1 day before the onset. Solar proton events, which may contaminate the electron channels, were removed from our event list using the NOAA Space Environment Center catalog of solar proton events. Furthermore, those events observed within 1 day by several different satellites are only counted as one event. Using this automated algorithm we selected 193 events.

Figure 1 shows an example from our electron flux dropout event list, which was observed by the GOES 13 satellite. As indicated by the ratio f_c/f_p, this electron flux dropout event occurred at ~05:00 UT on 17 September 2011 and lasted until ~16:00 UT, during which both the electron fluxes with energies $E > 0.6$ MeV and $E > 2$ MeV decreased by about 2 orders of magnitude within ~11 h (Figure 1c). The levels of electron fluxes remained low for the following several days, even after the geomagnetic condition recovered to the predropout level on 19 September, indicating that there was a real and permanent loss of relativistic electrons at GEO. This dropout event occurred during a modest geomagnetic storm with a

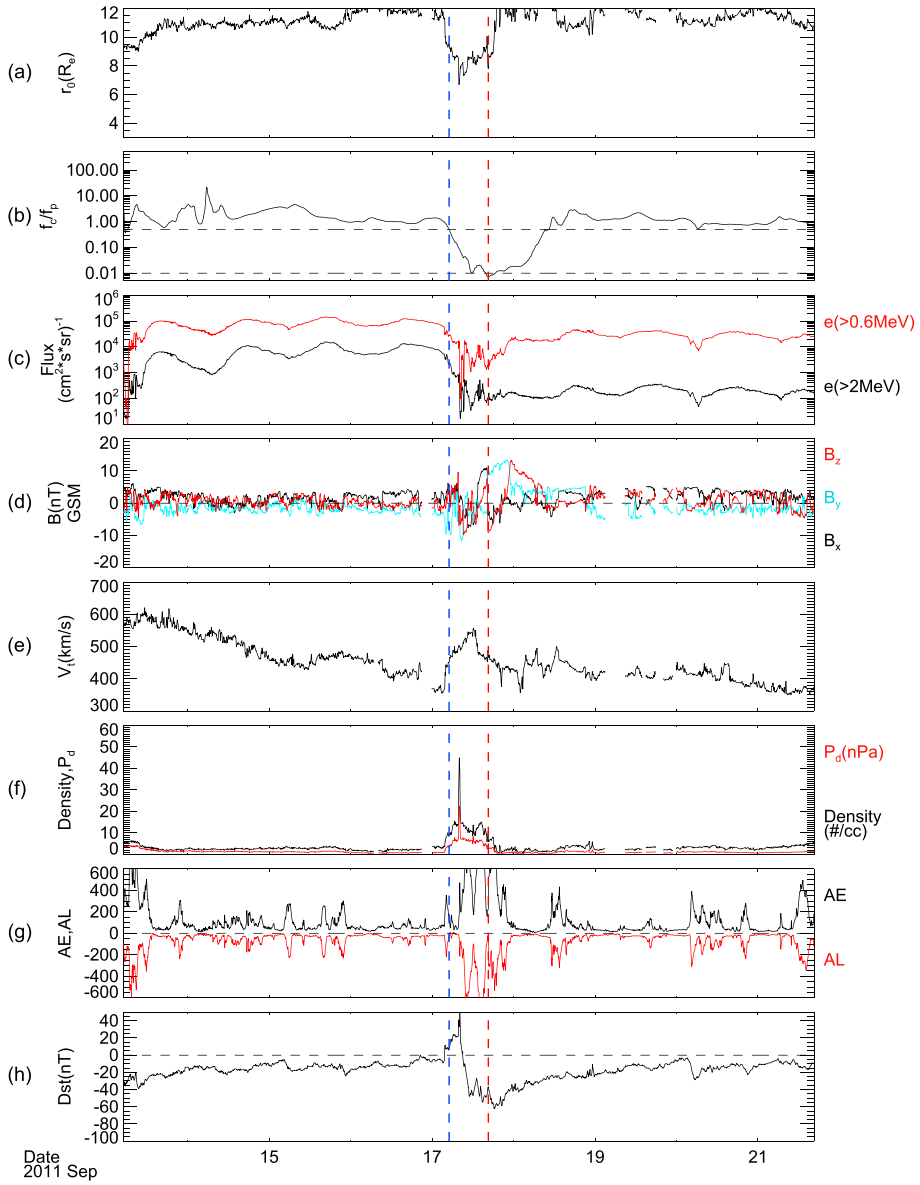

Figure 1. An example of a relativistic electron flux dropout event detected by the GOES 13 satellite on 17 September 2011 showing (a) the modeled subsolar magnetopause location r_0 [*Shue et al.*, 1998], (b) the ratio between the electron (>2 MeV) flux at the current time f_c and that of its previous day f_p with two horizontal dashed lines indicating the values of 0.5 and 0.01, (c) the absolute electron fluxes at geosynchronous orbit with energies $E > 0.6$ MeV (red line) and $E > 2$ MeV (black line), (d) three components (B_x, B_y, and B_z) of IMF in GSM coordinates, (e) total solar wind speed V_t, (f) solar wind dynamic pressure P_d (red line) and density (black line), (g) *AE* (black line) and *AL* (red line), and (h) *Dst* index. The onset and end of the dropout event are marked by the vertical blue and red dashed lines, respectively.

minimum *Dst* index of ~ −60 nT (Figure 1h). The onset of this dropout event was triggered by a substantial increase in solar wind dynamic pressure (Figure 1f), which causes the strong inward motion of the magnetopause close to GEO, as can be seen with the aid of the empirical subsolar magnetopause location (Figure 1a). The reversal of IMF B_z from northward to southward is also observed in Figure 1d, which is closely associated with the strong disturbance in the *AE* and *AL* indices (Figure 1g) owing to strong injections from the plasma sheet.

Solar wind dynamic pressure P_d and IMF B_z are believed to play the most significant role in triggering the electron flux dropout and are therefore chosen to classify the dropout events in our study. We use the instantaneous maximum dynamic pressure P_{max} during each dropout event (from onset to end) to

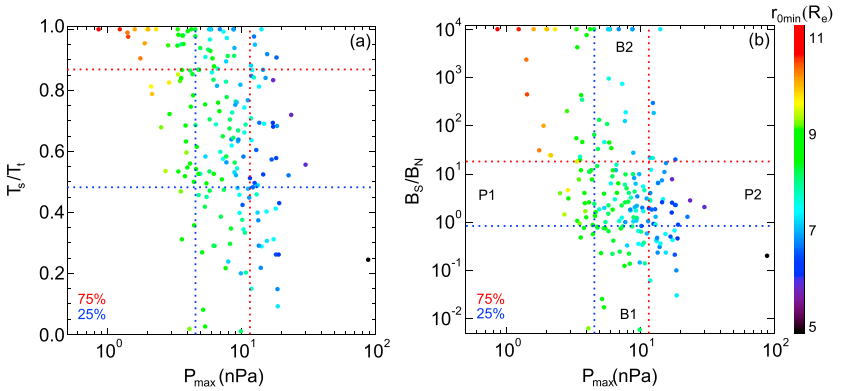

Figure 2. The distributions of the dropout events in the (a) T_s/T_t-P_{max} and (b) B_S/B_N-P_{max} domains, respectively. In two panels, each solid circle represents one dropout event, and its color denotes the minimum magnetopause location (r_{0min}) during the dropout event. The blue and red dotted lines show the first (25%) and third (75%) quartiles, respectively.

represent the magnitude of the solar wind dynamic pressure. However, two proxies are used to classify the southward IMF B_z: (1) T_s/T_t, which is the percentage of time duration with the southward IMF B_z during each dropout event; (2) B_S/B_N, which is the ratio of the sum of the absolute magnitude of southward IMF B_z to that of northward IMF B_z during each dropout event. Note that if the IMF B_z remains continuously southward during one dropout event, B_S/B_N is artificially set to 10^4 in this study for convenience. Figure 2 displays the distributions of the dropout events in the (a) T_s/T_t-P_{max} and (b) B_S/B_N-P_{max} domains, respectively. In the two panels, each solid circle represents one dropout event, and its color denotes the minimum magnetopause location (r_{0min}) during the dropout event calculated using the *Shue et al.* [1998] model. The blue and red dotted lines show the first (25%) and third (75%) quartiles, respectively. In both panels, these dropout events seem to be spread along a line from top left to bottom right, which suggests that both the southward IMF B_z and large solar wind dynamic pressure are important, and either one can solely result in a significant electron flux dropout. Moreover, the dropout events can occur not only when the magnetopause is pushed inward significantly ($r_{0min} < 6\ R_E$) but also when the magnetopause is quite far ($r_{0min} > 10\ R_E$). In Figure 2, it is shown that some dropout events take place with r_{0min}~11 R_E, during which the solar wind dynamic pressure is very small. This indicates that the magnetopause is not the only place where the relativistic electrons can be lost, and therefore, not all the dropout events can be explained by the magnetopause shadowing. Surprisingly, there are still four events detected with the condition that the solar wind dynamic pressure is low and the IMF B_z is northward as shown in the bottom left of two panels. Although the cause of dropout in these events may be very interesting, it is beyond the scope of this paper and will be left for a future study.

In order to isolate and investigate the roles of the solar wind dynamic pressure and IMF B_z, four groups (P1, P2, B1, and B2 shown in Figure 2b) of relativistic electron dropout events are chosen to conduct the superposed epoch analysis. The boundaries between the four groups (P1, P2, B1, and B2) are the first (25%) and third (75%) quartiles. The dropout events in Groups P1 and P2 occur with a similar IMF B_z, but with the significantly different solar wind dynamic pressure. Similarly, Groups B1 and B2 are compared to isolate and show the effects primarily driven by the southward IMF B_z.

3.2. Superposed Epoch Analysis

The superposed epoch analysis triggered by the onset of dropout events is conducted on the relativistic electron dropout events in the four groups (P1, P2, B1, and B2) selected above. Figure 3 presents the averaged results of superposed epoch analyses for the subsolar magnetopause location r_0, electron fluxes with energies $E > 0.6$ MeV and $E > 2$ MeV at GEO, IMF B_z, solar wind total speed V_t, density, dynamic pressure P_d, *AE*, *Dst*, and *Kp* for Groups (a) P1 and (b) P2, respectively. The zero epoch is the onset of dropout events and denoted by vertical dashed lines. Note that the electron fluxes were normalized by the mean flux of 1 day prior to the onset for each event before conducting the superposed epoch analysis. As a result, any potential nonphysical effects on the superposition, which are caused by the different

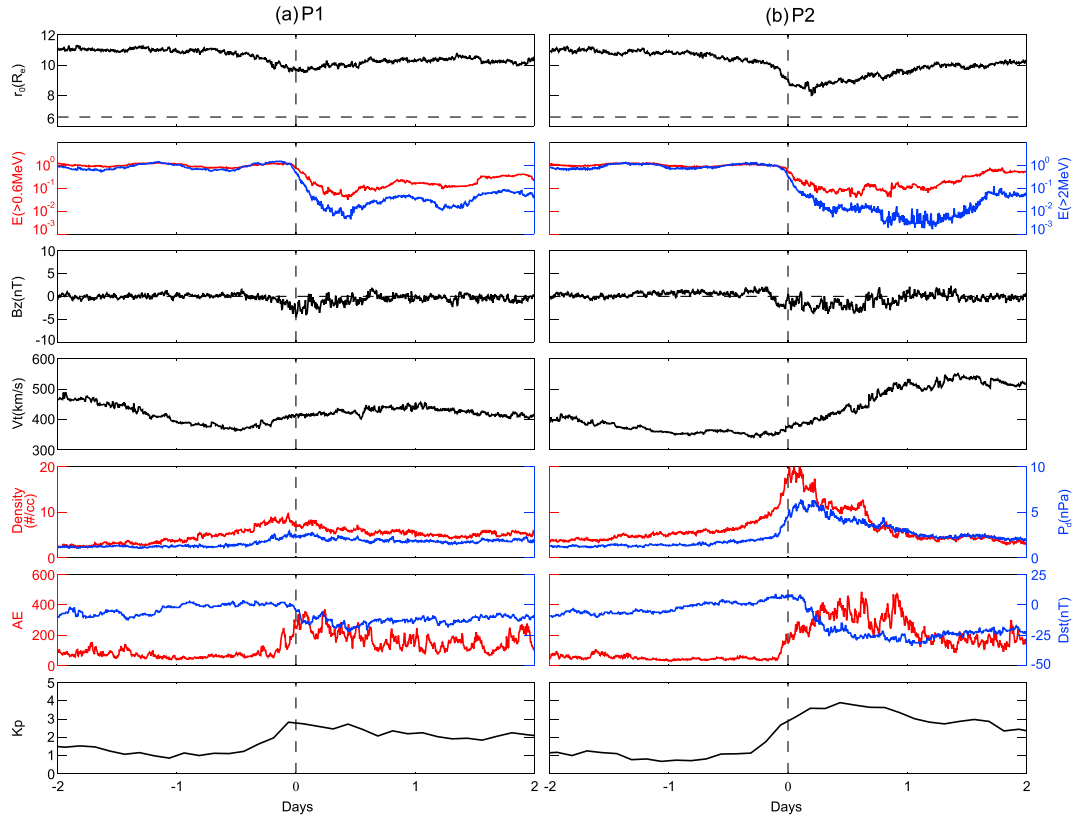

Figure 3. The superposed averages of the subsolar magnetopause locations r_0, electron fluxes with energies $E > 0.6$ MeV (red) and $E > 2$ MeV (blue) at GEO, IMF B_z, solar wind speed V_t, density (red), dynamic pressure P_d (blue), *AE* (red), *Dst* (blue), and *Kp* for Groups (a) P1 and (b) P2, respectively. The zero epoch is the onset of dropout events and denoted by vertical black dashed lines.

instruments onboard different satellites, can be eliminated. Prior to the onset, the electron flux experiences the diurnal variation in response to the change of magnetic field topology, with its minimum at midnight and maximum at noon. However, at the zero epoch, the electron fluxes with energy values $E > 0.6$ MeV and $E > 2$ MeV begin to decrease rapidly and continue to drop by 1 and 2 orders of magnitude, respectively, within 1 day. Moreover, the averaged electron fluxes of Group P2 decrease more significantly than those of Group P1, especially for the electrons with higher energies. This can also be found in Figure 4. Comparing P1 and P2, the IMF B_z evolution is quite similar only with a small southward component (~ -3 nT) around the onset, while the solar wind dynamic pressure is much larger in P2 due to the sudden increase of the solar wind speed and density. Consequently, the averaged magnetopause location of Group P2 is much closer to the Earth than that of Group P1, leading to the minimum at about 8 R_E. It is worth noting that in individual events the minimum magnetopause location could be much closer than the superposed average value owing to variations in the timing of the minima. As shown in Figure 2b, the minimum magnetopause location during the dropout events in Group P2 mostly can reach the geosynchronous orbit. However, compared with P1, the larger solar wind dynamic pressure in P2 only causes the slightly larger geomagnetic indices, such as *AE*, *Dst*, and *Kp*.

Figure 4 shows the results of the superposed epoch analysis of dropout events in Groups (a) P1 and (b) P2 for the T90 and T0 measurements of electrons with energies $E > 30$ keV, $E > 100$ keV, $E > 300$ keV, and $E > 1$ MeV averaged over all MLT sectors. The bin size is 0.5 L × 1 h. The zero epoch is the onset of dropout events and is denoted by vertical dashed lines. The superposed average of the magnetopause location (black line) is also overplotted for reference in each panel. In the fifth row, the two panels illustrate the normalized flux of trapped electrons with energy $E > 1$ MeV, which is obtained by dividing the electron flux by the mean flux occurring 24 h prior to the onset (zero epoch) at the same L shell. We discard those bins with the trapped

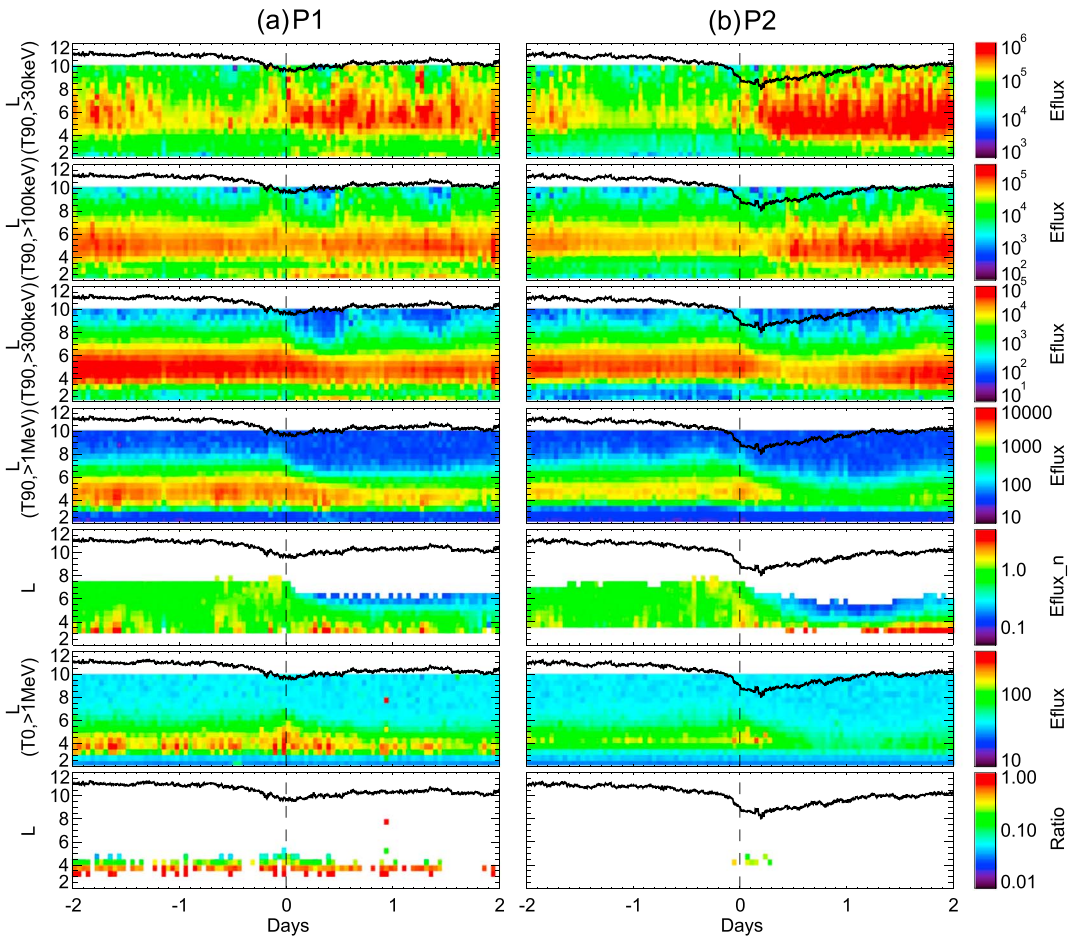

Figure 4. The superposed averages of the T90 and T0 measurements for electrons with energies $E > 30$ keV, $E > 100$ keV, $E > 300$ keV, and $E > 1$ MeV for dropout events in Groups (a) P1 and (b) P2. The bin size is 0.5 L × 1 h. The zero epoch is the onset of dropout events and denoted by vertical dashed lines. The black line in each panel shows the superposed average of the magnetopause location.

electron flux smaller than 150 $cm^{-2}\,s^{-1}\,sr^{-1}$, which is close to the background level. The ratio displayed in bottom panels is the ratio between the flux of precipitating electrons to that of trapped electrons with energy $E > 1$ MeV in the same bin and is calculated for the bins where the flux of precipitating electrons is larger than 150 $cm^{-2}\,s^{-1}\,sr^{-1}$. Compared with the results of P1 in Figure 4a, the fluxes of trapped electrons in all energy channels (from the top row to the forth row) in Figure 4b exhibit a faster and more significant depletion just after the onset. The fluxes of trapped electrons with lower energies recover very quickly, which is probably due to the injections of energetic electrons from the plasma sheet. However, electron flux enhancements for higher energy (approximately MeV) electrons take longer time (a few to ~10 h) through the local acceleration by chorus waves [e.g., *Thorne et al.*, 2013], which may account for the slow recovery of the relativistic electron flux. For trapped electrons with energy value $E > 1$ MeV, the flux dropout (drop by at least 1 order of magnitude) can be detected deep into L~4.5 in P2, much closer than L~6 in P1, as shown in the fifth row. However, there is no such difference between Groups P1 and P2 in the flux of precipitating relativistic electrons. Both the flux of precipitating electrons (sixth row) and the ratio (seventh row) between the flux of precipitating and trapped electrons are quite low in Groups P1 and P2, which indicates that the precipitation of relativistic electrons into the Earth's atmosphere is probably not able to account for the flux dropout of relativistic electrons, consistent with the findings of *Meredith et al.* [2011]. Here the abnormally strong >1 MeV electron precipitation in P1 below L~4 is due to contamination by the energetic protons, which was too difficult to remove. We have checked the flux of protons with energies >16 MeV in the four groups (not shown here) and clearly find that the energetic proton flux in Group P1 is most significant, especially below L~4, although we have removed solar proton

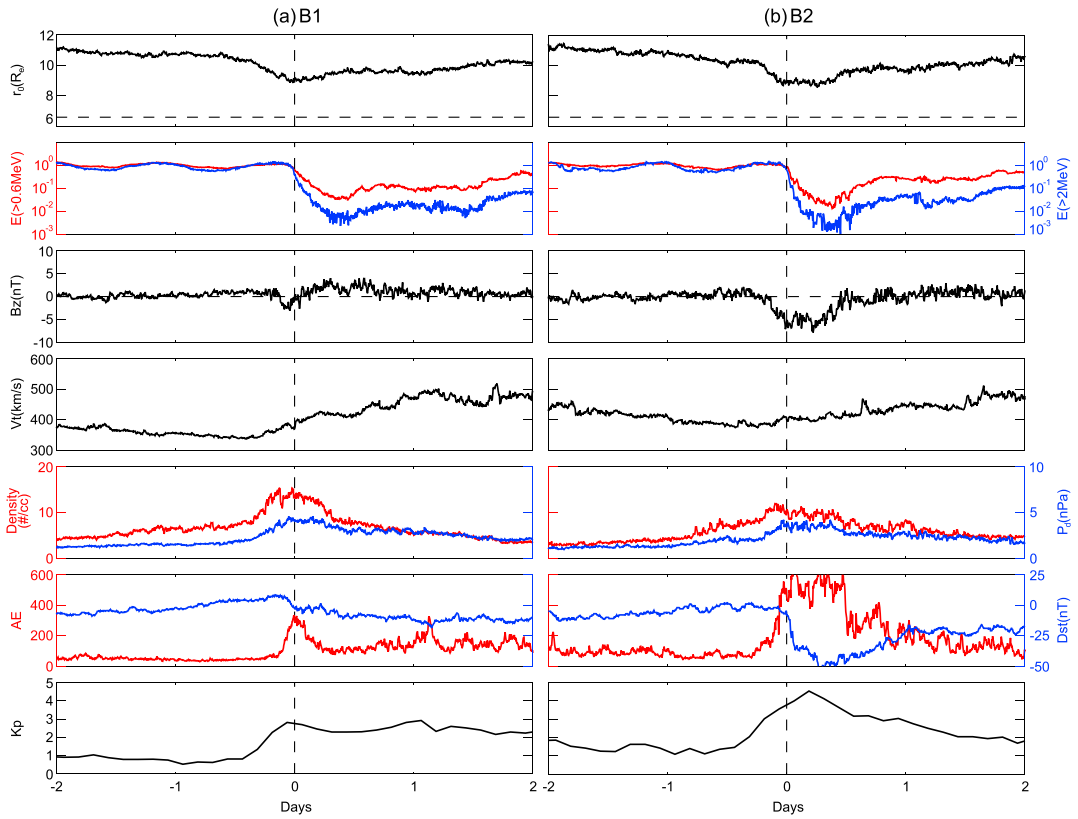

Figure 5. The superposed results for Groups B1 and B2 with the same format as Figure 3.

events based on the NOAA Space Environment Center catalog. Moreover, there is a clear consistency between the abnormally strong >1 MeV electron precipitation below L~4 and the energetic proton flux. The strong energetic proton flux may be due to the enhanced solar activity, but it still needs further investigation and is beyond the scope of this paper. Overall, from Figures 3 and 4, we find that larger solar wind dynamic pressure pushes the magnetopause to progressively lower radial locations and leads to more significant flux dropouts of relativistic electrons.

The superposed epoch analysis results of Groups B1 and B2 are displayed in Figure 5 with the same format as Figure 3. Both the superposed results of Groups B1 and B2 show a moderate solar wind dynamic pressure P_d (~3 nPa) and roughly similar subsolar magnetopause locations r_0 (>9 R_E) near the onset. But the IMF B_z (third row) in Figure 5b is observed turning southward just prior to the onset and then reaching about −8 nT over several hours. The strong southward IMF B_z can result in the significant magnetospheric convection and the strong injections from the plasma sheet, which is also reflected in the much more disturbed *Dst*, and much larger *AE* and *Kp* in Figure 5b. This means that the relativistic electron dropout events in Group B2 occur during geomagnetically active periods. Overall, the dropout of electron fluxes with energy values $E > 0.6$ MeV and $E > 2$ MeV is more significant but the electron fluxes recover more quickly in B2 than B1, which is also shown in Figure 6. The faster recovery is probably due to the elevated level of convection and substorm activity [e.g., *McPherron et al.*, 2009; *Li et al.*, 2012], which provide the source and seed electrons to generate whistler mode chorus waves, which in turn accelerate ~100 keV seed electrons to >1 MeV [e.g., *Horne et al.*, 2005; *Thorne et al.*, 2013].

Figure 6 has the same format as Figure 4, which illustrates the superposed average of electron measurements by POES for Groups B1 and B2. In Figure 6a, the fluxes of trapped electrons in higher-energy channels ($E > 300$ keV and $E > 1$ MeV) show a moderate depletion, which is obvious at the large L shell (L > 5.5). However, in Figure 6b, the fluxes of trapped electrons in lower-energy channels ($E > 30$ keV and $E > 100$ keV) do not exhibit any depletion at the zero epoch. Instead, they experience a rapid increase over a large range of L shells (from 3 to 9), which is likely due to a series of strong injections from the plasma

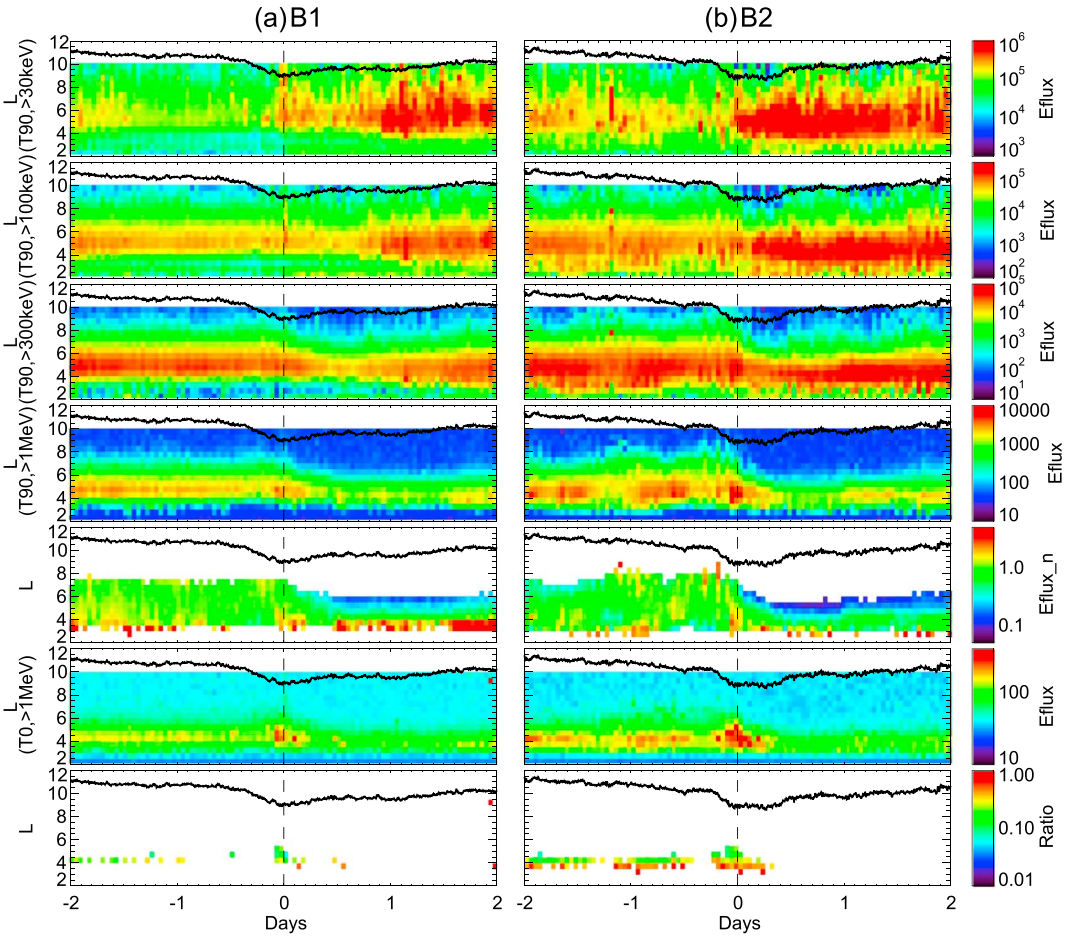

Figure 6. The superposed results for Groups B1 and B2 with the same format as Figure 4.

sheet, as indicated by the large *AE* index in Figure 5b. The most evident flux dropout of trapped electrons is found in the energy channel $E > 1$ MeV within a 0.3 day interval after the zero epoch, which can penetrate into much lower L shells (L~4.5). The subsequent electron depletion is significantly weaker and lasts nearly for 1 day. This might be due to the much weaker electron precipitation, which is probably close to the background noise level and thus cannot be measured by POES particle detectors. The relatively gradual recovery of the relativistic electron flux (>1 MeV) may be caused by the local acceleration driven by whistler mode chorus waves. More importantly, the flux of precipitating electrons with energies $E > 1$ MeV shows a notable difference between Groups B1 and B2. Both the flux of precipitating electrons (sixth row) and the ratio (bottom row) between the flux of precipitating and trapped electrons are much larger with the passage of the large southward IMF B_z, as shown in Figure 6b.

The dependence of relativistic electron precipitation on the magnetic local time (MLT) is also investigated next. Figure 7 shows the superposed average of the trapped and precipitating electron fluxes, and the ratio between them for Group B2 in the dawn ($3\,\text{h} < \text{MLT} < 9\,\text{h}$), noon ($9\,\text{h} < \text{MLT} < 15\,\text{h}$), dusk ($15\,\text{h} < \text{MLT} < 21\,\text{h}$), and midnight ($\text{MLT} > 21\,\text{h}$ or $\text{MLT} < 3\,\text{h}$) sectors. The zero epoch is the onset of flux dropout events and denoted by vertical dashed lines. Following the same approach as Figures 4 and 6, the ratio is calculated only in the bins where the flux of precipitating electrons is larger than $150\,\text{cm}^{-2}\,\text{s}^{-1}\,\text{sr}^{-1}$. In the dawn and noon sectors, there is almost no electron precipitation near the onset. However, in the dusk sector, both the flux of precipitating electrons and the ratio between the flux of precipitating electrons to trapped electrons become very significant along with the onset of dropouts in the range of $4 < \text{L} < 6$. Meanwhile, it is worth noting that the local bounce loss cone at the altitude of POES/MetOp satellites is ~59°, which is much larger than the field of view of T0 (~30°). As a result, only a

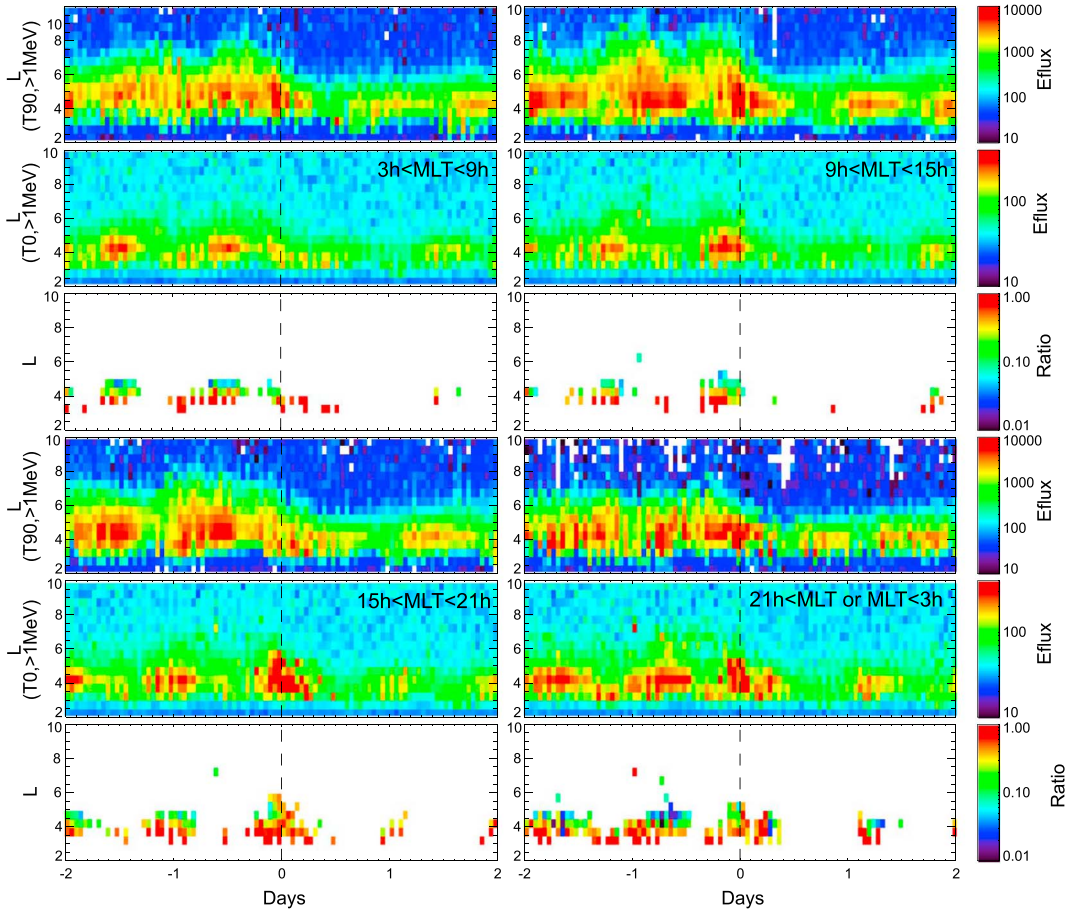

Figure 7. The superposed averages of the fluxes of trapped and precipitating electrons, and the ratio between them for Group B2 in dawn (3 h < MLT < 9 h), noon (9 h < MLT < 15 h), dusk (15 h < MLT < 21 h), and midnight (MLT > 21 h or MLT < 3 h) sectors. The zero epoch is the time at the onset of the flux dropout events and denoted by vertical dashed lines.

small part of the precipitating flux of relativistic electrons is measured, and the actual precipitation could be even stronger, which may account for the global dropouts of relativistic electrons. One other thing to note is that during the strong injections, the electromagnetic ion cyclotron waves (EMIC waves) are usually observed in the dusk sector, with large wave amplitudes (> ~ 1 nT) [*Halford et al.*, 2010; *Usanova et al.*, 2012]. Both theoretical and simulation studies have confirmed that EMIC waves play an important role in resonant scattering of energetic radiation belt electrons into the loss cone and causing the atmospheric precipitation of relativistic electrons [*Li et al.*, 2007; *Jordanova et al.*, 2008; *Carson et al.*, 2013; *Wang et al.*, 2014]. Therefore, the enhancement of precipitating flux of relativistic electrons at the onset of dropouts may be due to the intense EMIC waves by strong injections of energetic ions from the plasma sheet. In addition, around the onset of dropouts, there are also modest relativistic electron precipitations in the midnight sector, although their flux and ratios are relatively lower. With the same format, Figure 8 presents the superposed results for Group P2. Similarly, there is almost no electron precipitation near the onset except for relatively weaker precipitation in the midnight sector. Compared to Figure 7, the precipitating fluxes of relativistic electrons in the dusk sector are too low to cause the relativistic electron flux dropout for Group P2, which suggests that during the large solar wind dynamic pressure, the relativistic electrons tend to escape from the magnetosphere rather than precipitate into the atmosphere.

4. Discussion

Based on our statistical results (Figure 2), we conclude that during most of the relativistic electron flux dropouts, both the high solar wind dynamic pressure and southward IMF B_z can potentially be important

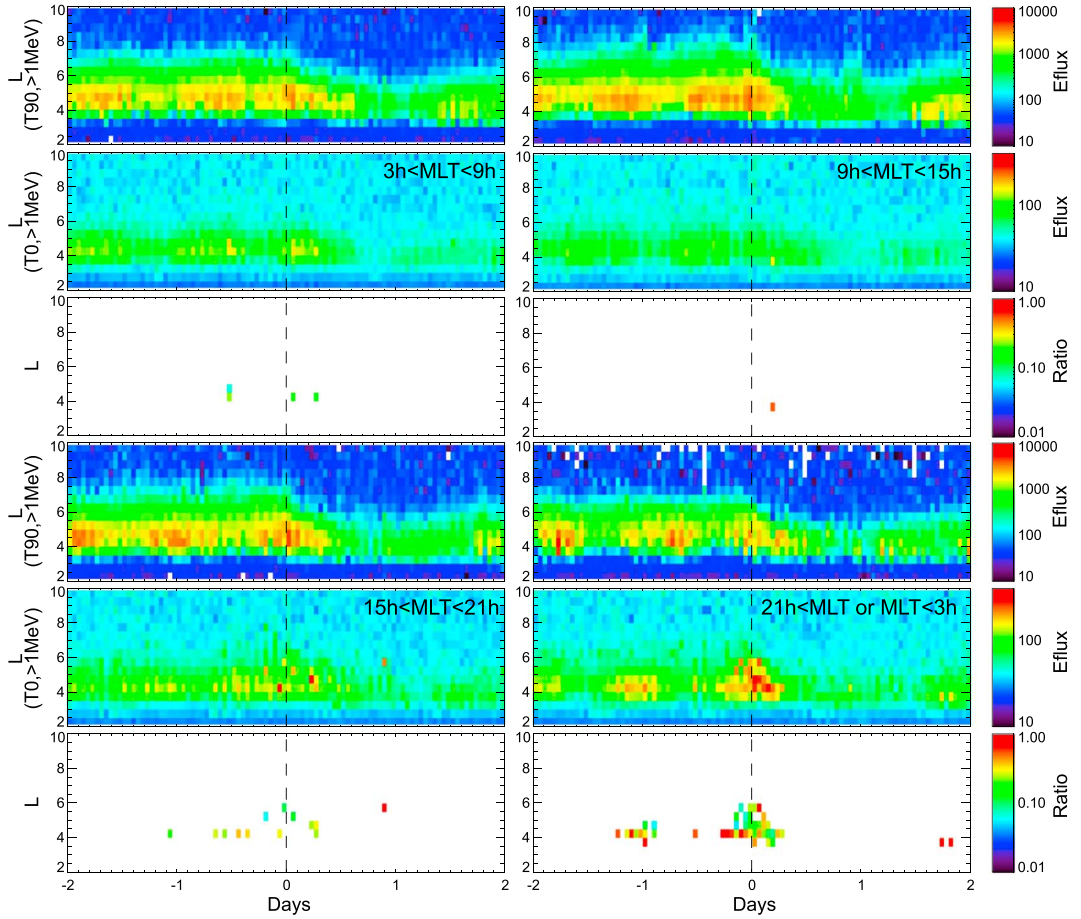

Figure 8. The superposed results for Group P2 with the same format as Figure 7.

due to the combined effects of magnetopause shadowing and pitch angle scattering loss. Those dropout events that occur during geomagnetic storms, which have been widely studied previously [*Denton and Borovsky*, 2008; *Borovsky and Denton*, 2009; *Meredith et al.*, 2011; *Yuan and Zong*, 2013], also have the difficulty of differentiating the distinct roles of the solar wind dynamic pressure and southward IMF B_z. As a result, either the magnetopause shadowing or wave-particle interaction has already been proposed to explain the relativistic electron flux dropouts, but no consensus has been reached. In order to investigate the roles of solar wind dynamic pressure and IMF B_z, we pick all the significant relativistic electron flux dropout events during the past ~16 years regardless of geomagnetic storms and then divide them into several groups according to the prevailing solar wind parameters. Comparing the events in Groups P1 and P2, which occur with similar IMF B_z, but with the distinct solar wind dynamic pressure, we surmise that the relativistic electrons are preferentially lost toward the magnetopause. Comparing the events in Groups B1 and B2, we find that the southward IMF B_z accounts for strong injections, which lead to the generation of intense waves (such as EMIC waves and chorus waves). Through wave-particle interactions, the relativistic electrons can be scattered into the loss cone and precipitate into the atmosphere. The remarkable precipitation flux of relativistic electrons in the dusk sector shown in Figure 7 further confirms this speculation.

EMIC waves are believed to be generated through unstable ring current ion distributions injected from the plasma sheet and observed primarily in the equatorial region of the magnetosphere. With the large southward IMF B_z and large *AE* index, the EMIC waves preferentially occur in the dusk sector with large amplitudes [*Erlandson and Ukhorskiy*, 2001; *Halford et al.*, 2010; *Usanova et al.*, 2012]. Moreover, their source region is also observed to extend to lower L shells with increasing storm intensity [*Bortnik et al.*, 2008].

Lyons and Thorne [1972] pointed out the anomalous resonant interactions of EMIC waves with relativistic electrons, which are able to scatter the electrons into the bounce loss cone through pitch angle scattering and thus cause precipitations into the atmosphere. Recently, both case studies and statistical results have provided observational evidence of the expected link between the EMIC waves and precipitating relativistic electrons [*Rodger et al.*, 2008; *Carson et al.*, 2013; *Wang et al.*, 2014]. However, whether the EMIC waves can result in the relativistic electron flux dropout is still under debate. In our study, with the large southward IMF B_z and *AE* index, the superposed results of Group B2 present the strong precipitation of relativistic electrons in the dusk sector, which is consistent with the preferential source region of EMIC waves based on previous observations [*Halford et al.*, 2010; *Usanova et al.*, 2012]. Our observational results support the idea that EMIC waves could significantly contribute to the relativistic electron flux dropouts.

Our results also show that there is relatively weak precipitation of relativistic electrons in the midnight sector with the large solar wind dynamic pressure or southward IMF B_z. Two potential mechanisms may be responsible. One is due to the scattering by EMIC waves. When the solar wind dynamic pressure is large or IMF B_z is continuously southward, the source region of the EMIC waves may extend to the midnight sector [*Usanova et al.*, 2012]. As a result, a small part of relativistic electrons can be scattered into the atmospheric loss cone by the EMIC waves. Another possibility is due to current sheet scattering, which occurs only when the electron gyroradius is comparable to the curvature radius of the local magnetic field. Either the large solar wind dynamic pressure or southward IMF B_z can intensify the ring current, which results in the more stretched magnetic fields in the midnight sector. In this case, the first adiabatic invariant of the relativistic electrons is violated. Subsequently, these relativistic electrons may scatter into the loss cone and precipitate into the atmosphere. To clearly understand the precipitation of relativistic electrons in the midnight sector, a further investigation is required, which is beyond the scope of this paper. During the event identification procedure, we initially found ~300 electron flux dropout events based on the method used in the study of *Green et al.* [2004]. However, there are some events during which the relativistic electron fluxes can recover to their predropout levels very fast ($<$1 day). We believe that those dropouts are probably caused predominantly by the adiabatic effect, i.e., "*Dst* effect." Since we focus on studying the real, permanent loss of relativistic electrons in this paper, the dropouts mainly due to the *Dst* effect should be eliminated. Therefore, an artificial criterion requiring that the mean electron flux 1 day after onset be significantly lower than that of 1 day before onset (e.g., 12.5%) was chosen to filter the initial event list, which has also been visually checked. It is worth noting that even in the final dropout events, the *Dst* effect still cannot be completely ruled out by using this artificial criterion but coexists with the real electron loss.

5. Summary

We have utilized the ~16 years of data from six polar-orbiting satellites (POES), eight geosynchronous spacecraft (GOES), and OMNIWEB solar wind database to study the roles played by the solar wind dynamic pressure and the southward IMF B_z in driving significant relativistic electron flux dropouts. This comprehensive analysis is performed for all significant relativistic electron flux dropouts regardless of the occurrence of geomagnetic storms. The principal results are summarized as follows:

1. Solar wind dynamic pressure and IMF B_z play key roles in causing the relativistic electron flux dropouts, and either a large solar wind dynamic pressure or a strong southward IMF B_z can solely result in the significant depletion of relativistic electrons.
2. The relativistic electron flux dropouts can occur not only when the magnetopause is compressed and moves closer to the Earth [*Bortnik et al.*, 2006; *Turner et al.*, 2012, 2014; *Yuan and Zong*, 2013] but also when the magnetopause is very far from the Earth. This indicates that the magnetopause is not the only place where the electrons can be lost and not all dropout events can be explained by the magnetopause shadowing alone.
3. The large solar wind dynamic pressure pushes the magnetopause inward strongly and causes the electrons to escape from the magnetosphere, which is consistent with previous works [*Bortnik*, 2006; *Turner et al.*, 2012, 2014; *Yuan and Zong*, 2013]. In addition, the continuous southward IMF B_z results in strong injections from the plasma sheet, which provides a source of free energy for electromagnetic wave excitation. Then through wave-particle interactions, the relativistic electrons can be scattered into the loss cone and precipitate into the atmosphere.

4. The most remarkable precipitation of relativistic electrons is observed in the dusk sector with the strong southward IMF B_z, where the EMIC waves are preferentially observed. Meanwhile, there is also weak precipitation of relativistic electrons in the midnight sector during either the strong southward IMF B_z or large dynamic pressure.

Acknowledgments

The work at USTC was supported by the National Science Foundation of China grants 41331067, 41474125, 41204103, and 11235009; 973 Program (2013CBA01503 and 2012CB825602); and CAS Key Research Program KZZD-EW-01-4. The analysis at UCLA was supported by the EMFISIS sub-award 1001057397:01; ECT sub-award 13–041; NASA grants NNX11AD75G, NNX11AR64G, NNX13AI61G, NNX14AI18G, and NNX15AF61G; NSF grant AGS 1405054; and the Air Force Young Investigator program. We acknowledge the GOES, POES, and OMNIWEB data used in this study obtained from http://satdat.ngdc.noaa.gov/sem/goes/data/, http://satdat.ngdc.noaa.gov/sem/poes/data/, and http://omniweb.gsfc.nasa.gov. We thank the World Data Center for Geomagnetism, Kyoto, for providing *Kp* index (http://wdc.kugi.kyoto-u.ac.jp/kp/index.html) used in this paper.

Michael Liemohn thanks the reviewers for their assistance in evaluating this paper.

References

Baker, D. N. (2002), How to cope with space weather, *Science*, *297*, 1486–1487, doi:10.1126/science.1074956.

Baker, D. N., and J. B. Blake (2012), SAMPEX: A long-serving radiation belt sentinel, in *Dynamics of the Earth's Radiation Belts and Inner Magnetosphere*, *Geophys. Monogr. Ser.*, vol. 199, pp. 21–40, AGU, Washington, D. C., doi:10.1029/2012GM001368.

Bargatze, L. F., R. L. McPherron, J. Minamora, and D. Weimer (2005), A new interpretation of Weimer et al.'s solar wind propagation delay technique, *J. Geophys. Res.*, *110*, A07105, doi:10.1029/2004JA010902.

Borovsky, J. E., and M. H. Denton (2009), Relativistic-electron dropouts and recovery: A superposed epoch study of the magnetosphere and the solar wind, *J. Geophys. Res.*, *114*, A02201, doi:10.1029/2008JA013128.

Borovsky, J. E., and M. H. Denton (2010), Magnetic field at geosynchronous orbit during high-speed stream-driven storms: Connections to the solar wind, the plasma sheet, and the outer electron radiation belt, *J. Geophys. Res.*, *115*, A08217, doi:10.1029/2009JA015116.

Bortnik, J., and R. M. Thorne (2007), The dual role of ELF/VLF chorus waves in the acceleration and precipitation of radiation belt electrons, *J. Atmos. Sol. Terr. Phys.*, *69*, 378–386, doi:10.1016/j.jastp.2006.05.030.

Bortnik, J., R. M. Thorne, T. P. O'Brien, J. C. Green, R. J. Strangeway, Y. Y. Shprits, and D. N. Baker (2006), Observation of two distinct, rapid loss mechanisms during the 20 November 2003 radiation belt dropout event, *J. Geophys. Res.*, *111*, A12216, doi:10.1029/2006JA011802.

Bortnik, J., J. W. Cutler, C. Dunson, T. E. Bleier, and R. L. McPherron (2008), Characteristics of low-latitude Pc1 pulsations during geomagnetic storms, *J. Geophys. Res.*, *113*, A04201, doi:10.1029/2007JA012867.

Carson, B. R., C. J. Rodger, and M. A. Clilverd (2013), POES satellite observations of EMIC-wave driven relativistic electron precipitation during 1998–2010, *J. Geophys. Res. Space Physics*, *118*, 232–243, doi:10.1029/2012JA017998.

Denton, M. H., and J. E. Borovsky (2008), Superposed epoch analysis of high-speed-stream effects at geosynchronous orbit: Hot plasma, cold plasma, and the solar wind, *J. Geophys. Res.*, *113*, A07216, doi:10.1029/2007JA012998.

Erlandson, R. E., and A. J. Ukhorskiy (2001), Observations of electromagnetic ion cyclotron waves during geomagnetic storms: Wave occurrence and pitch angle scattering, *J. Geophys. Res.*, *106*, 3883–3895, doi:10.1029/2000JA000083.

Evans, D. S., and M. S. Greer (2004), Polar Orbiting Environmental Satellite Space Environment Monitor-2: Instrument descriptions and archive data documentation, NOAA Tec. Mem. 93, version 1.4, Space Weather Predict. Cent., Boulder, Colo.

Freden, S. C., and R. S. White (1960), Particle fluxes in the inner radiation belt, *J. Geophys. Res.*, *65*, 1377–1383, doi:10.1029/JZ065i005p01377.

Green, J. C. (2013), *MEPED Telescope Data Processing Algorithm Theoretical Basis Document*, Natl. Oceanic and Atmos. Admin. Space Environ. Cent, Boulder, Colo.

Green, J. C., T. G. Onsager, T. P. O'Brien, and D. N. Baker (2004), Testing loss mechanisms capable of rapidly depleting relativistic electron flux in the Earth's outer radiation belt, *J. Geophys. Res.*, *109*, A12211, doi:10.1029/2004JA010579.

Halford, A. J., B. J. Fraser, and S. K. Morley (2010), EMIC wave activity during geomagnetic storm and nonstorm periods: CRRES results, *J. Geophys. Res.*, *115*, A12248, doi:10.1029/2010JA015716.

Horne, R. B., et al. (2005), Wave acceleration of electrons in the Van Allen radiation belts, *Nature*, *437*, 227–230, doi:10.1038/nature03939.

Imhof, W. L., H. D. Voss, J. Mobilia, D. W. Datlowe, and E. E. Gaines (1991), The precipitation of relativistic electrons near the trapping boundary, *J. Geophys. Res.*, *96*, 5619–5629, doi:10.1029/90JA02343.

Jordanova, V. K., J. Albert, and Y. Miyoshi (2008), Relativistic electron precipitation by EMIC waves from self-consistent global simulations, *J. Geophys. Res.*, *113*, A00A10, doi:10.1029/2008JA013239.

Kim, K. C., D. Y. Lee, H. J. Kim, E. S. Lee, and C. R. Choi (2010), Numerical estimates of drift loss and Dst effect for outer radiation belt relativistic electrons with arbitrary pitch angle, *J. Geophys. Res.*, *115*, A03208, doi:10.1029/2009JA014523.

Kim, K. C., D. Y. Lee, Y. Shprits, H. J. Kim, and E. Lee (2011), Electron flux changes in the outer radiation belt by radial diffusion during the storm recovery phase in comparison with the fully adiabatic evolution, *J. Geophys. Res.*, *116*, A09229, doi:10.1029/2011JA016642.

Lam, M. M., R. B. Horne, N. P. Meredith, S. A. Glauert, T. Moffat-Griffin, and J. C. Green (2010), Origin of energetic electron precipitation >30 keV into the atmosphere, *J. Geophys. Res.*, *115*, A00F08, doi:10.1029/2009JA014619.

Li, W., Y. Y. Shprits, and R. M. Thorne (2007), Dynamic evolution of energetic outer zone electrons due to wave-particle interactions during storms, *J. Geophys. Res.*, *112*, A10220, doi:10.1029/2007JA012368.

Li, W., R. Thorne, J. Bortnik, R. McPherron, Y. Nishimura, V. Angelopoulos, and I. G. Richardson (2012), Evolution of chorus waves and their source electrons during storms driven by corotating interaction regions, *J. Geophys. Res.*, *117*, A08209, doi:10.1029/2012JA017797.

Li, W., et al. (2014), Radiation belt electron acceleration by chorus waves during the 17 March 2013 storm, *J. Geophys. Res. Space Physics*, *119*, 4681–4693, doi:10.1002/2014JA019945.

Lyons, L. R., and R. M. Thorne (1972), Parasitic pitch angle diffusion of radiation belt particles by ion-cyclotron waves, *J. Geophys. Res.*, *77*, 5608–5616, doi:10.1029/JA077i028p05608.

Maalouf, M., M. Durante, and N. Foray (2011), Biological effects of space radiation on human cells: History, advances and outcomes, *J. Radiat. Res.*, *52*, 126–146, doi:10.1269/Jrr.10128.

Mcilwain, C. E. (1966), Ring current effects on trapped particles, *J. Geophys. Res.*, *71*, 3623–3628, doi:10.1029/JZ071i015p03623.

McPherron, R. L., D. N. Baker, and N. U. Crooker (2009), Role of the Russell-McPherron effect in the acceleration of relativistic electrons, *J. Atmos. Sol. Terr. Phys.*, *71*, 1032–1044, doi:10.1016/j.jastp.2008.11.002.

Meredith, N. P., R. B. Horne, M. M. Lam, M. H. Denton, J. E. Borovsky, and J. C. Green (2011), Energetic electron precipitation during high-speed solar wind stream driven storms, *J. Geophys. Res.*, *116*, A05223, doi:10.1029/2010JA016293.

Millan, R. M., and R. M. Thorne (2007), Review of radiation belt relativistic electron losses, *J. Atmos. Sol. Terr. Phys.*, *69*, 362–377, doi:10.1016/j.jastp.2006.06.019.

Millan, R. M., R. P. Lin, D. M. Smith, and M. P. McCarthy (2007), Observation of relativistic electron precipitation during a rapid decrease of trapped relativistic electron flux, *Geophys. Res. Lett.*, *34*, L10101, doi:10.1029/2006GL028653.

Morley, S. K., R. H. W. Friedel, T. E. Cayton, and E. Noveroske (2010a), A rapid, global and prolonged electron radiation belt dropout observed with the Global Positioning System constellation, *Geophys. Res. Lett.*, *37*, L06102, doi:10.1029/2010GL042772.

Morley, S. K., R. H. W. Friedel, E. L. Spanswick, G. D. Reeves, J. T. Steinberg, J. Koller, T. Cayton, and E. Noveroske (2010b), Dropouts of the outer electron radiation belt in response to solar wind stream interfaces: Global positioning system observations, *Proc. R. Soc. A*, *466*, 3329–3350, doi:10.1098/rspa.2010.0078.

Ohtani, S., Y. Miyoshi, H. J. Singer, and J. M. Weygand (2009), On the loss of relativistic electrons at geosynchronous altitude: Its dependence on magnetic configurations and external conditions, *J. Geophys. Res.*, *114*, A01202, doi:10.1029/2008JA013391.

Onsager, T. G., et al. (1996), Operational uses of the GOES energetic particles detectors, in *GOES-8 and Beyond*, edited by E. R. Washwell, *SPIE Conf. Proc.*, *2812*, 281–290.

Onsager, T. G., G. Rostoker, H. J. Kim, G. D. Reeves, T. Obara, H. J. Singer, and C. Smithtro (2002), Radiation belt electron flux dropouts: Local time, radial, and particle-energy dependence, *J. Geophys. Res.*, *107*(A11), 1382, doi:10.1029/2001JA000187.

Parker, E. N. (1960), Geomagnetic fluctuations and the form of the outer zone of the Van Allen radiation belt, *J. Geophys. Res.*, *65*, 3117–3130, doi:10.1029/JZ065i010p03117.

Randall, C. E., et al. (2005), Stratospheric effects of energetic particle precipitation in 2003–2004, *Geophys. Res. Lett.*, *32*, L05802, doi:10.1029/2004GL022003.

Reeves, G. D., K. L. McAdams, R. H. W. Friedel, and T. P. O'Brien (2003), Acceleration and loss of relativistic electrons during geomagnetic storms, *Geophys. Res. Lett.*, *30*(10), 1529, doi:10.1029/2002GL016513.

Rodger, C. J., T. Raita, M. A. Clilverd, A. Seppala, S. Dietrich, N. R. Thomson, and T. Ulich (2008), Observations of relativistic electron precipitation from the radiation belts driven by EMIC waves, *Geophys. Res. Lett.*, *35*, L16106, doi:10.1029/2008GL034804.

Rodger, C. J., M. A. Clilverd, J. C. Green, and M. M. Lam (2010), Use of POES SEM-2 observations to examine radiation belt dynamics and energetic electron precipitation into the atmosphere, *J. Geophys. Res.*, *115*, A04202, doi:10.1029/2008JA014023.

Sandanger, M. I., F. Soraas, M. Sorbo, K. Aarsnes, K. Oksavik, and D. S. Evans (2009), Relativistic electron losses related to EMIC waves during CIR and CME storms, *J. Atmos. Sol. Terr. Phys.*, *71*, 1126.

Selesnick, R. S., and S. G. Kanekal (2009), Variability of the total radiation belt electron content, *J. Geophys. Res.*, *114*, A02203, doi:10.1029/2008JA013432.

Sergeev, V. A., and N. A. Tsyganenko (1982), Energetic particle losses and trapping boundaries as deduced from calculations with a realistic magnetic-field model, *Planet. Space Sci.*, *30*, 999–1006, doi:10.1016/0032-0633(82)90149-0.

Shprits, Y. Y., R. M. Thorne, R. Friedel, G. D. Reeves, J. Fennell, D. N. Baker, and S. G. Kanekal (2006), Outward radial diffusion driven by losses at magnetopause, *J. Geophys. Res.*, *111*, A11214, doi:10.1029/2006JA011657.

Shprits, Y. Y., D. Subbotin, and B. Ni (2009), Evolution of electron fluxes in the outer radiation belt computed with the VERB code, *J. Geophys. Res.*, *114*, A11209, doi:10.1029/2008JA013784.

Shprits, Y. Y., M. Daae, and B. Ni (2012), Statistical analysis of phase space density buildups and dropouts, *J. Geophys. Res.*, *117*, A01219, doi:10.1029/2011JA016939.

Shue, J.-H., et al. (1998), Magnetopause location under extreme solar wind conditions, *J. Geophys. Res.*, *103*(A8), 17,691–17,700, doi:10.1029/98JA01103.

Summers, D., B. Ni, and N. P. Meredith (2007), Timescales for radiation belt electron acceleration and loss due to resonant wave-particle interactions: 2. Evaluation for VLF chorus, ELF hiss, and electromagnetic ion cyclotron waves, *J. Geophys. Res.*, *112*, A04207, doi:10.1029/2006JA011993.

Thorne, R. M. (2010), Radiation belt dynamics: The importance of wave-particle interactions, *Geophys. Res. Lett.*, *37*, L22107, doi:10.1029/2010GL044990.

Thorne, R. M., and C. F. Kennel (1971), Relativistic electron precipitation during magnetic storm main phase, *J. Geophys. Res.*, *76*, 4446–4453, doi:10.1029/JA076i019p04446.

Thorne, R. M., T. P. O'Brien, Y. Y. Shprits, D. Summers, and R. B. Horne (2005), Timescale for MeV electron microburst loss during geomagnetic storms, *J. Geophys. Res.*, *110*, A09202, doi:10.1029/2004JA010882.

Thorne, R. M., et al. (2013), Rapid local acceleration of relativistic radiation-belt electrons by magnetospheric chorus, *Nature*, *504*, 411–414, doi:10.1038/Nature12889.

Turner, D. L., Y. Shprits, M. Hartinger, and V. Angelopoulos (2012), Explaining sudden losses of outer radiation belt electrons during geomagnetic storms, *Nat. Phys.*, *8*, 208–212, doi:10.1038/Nphys2185.

Turner, D. L., et al. (2014), On the cause and extent of outer radiation belt losses during the 30 September 2012 dropout event, *J. Geophys. Res. Space Physics*, *119*, 1530–1540, doi:10.1002/2013JA019446.

Usanova, M. E., I. R. Mann, J. Bortnik, L. Shao, and V. Angelopoulos (2012), THEMIS observations of electromagnetic ion cyclotron wave occurrence: Dependence on AE, SYMH, and solar wind dynamic pressure, *J. Geophys. Res.*, *117*, A10218, doi:10.1029/2012JA018049.

Van Allen, J. A., and L. A. Frank (1959), Radiation around the Earth to a radial distance of 107,400 km, *Nature*, *183*, 430–434, doi:10.1038/183430a0.

Wang, Z. Z., Z. G. Yuan, M. Li, H. M. Li, D. D. Wang, H. M. Li, S. Y. Huang, and Z. Qiao (2014), Statistical characteristics of EMIC wave-driven relativistic electron precipitation with observations of POES satellites: Revisit, *J. Geophys. Res. Space Physics*, *119*, 5509–5519, doi:10.1002/2014JA020082.

Weimer, D. R., and J. H. King (2008), Improved calculations of interplanetary magnetic field phase front angles and propagation time delays, *J. Geophys. Res.*, *113*, A01105, doi:10.1029/2007JA012452.

Yuan, C. J., and Q. G. Zong (2013), Relativistic electron fluxes dropout in the outer radiation belt under different solar wind conditions, *J. Geophys. Res. Space Physics*, *118*, 7545–7556, doi:10.1002/2013JA019066.